

Molecular Counterparts of Ultracompact HII Regions with Extended Envelopes

Kee-Tae Kim^{1,2} and Bon-Chul Koo²

ABSTRACT

We have carried out ^{13}CO J=1–0, CS, and C^{34}S J=2–1 and J=3–2 line observations of molecular clouds associated with 16 ultracompact (UC) HII regions with extended envelopes. The molecular clouds are the ones that give birth to rich stellar clusters and/or very massive (O7–O4) stars. Our data show that the clouds are very clumpy and of irregular morphology. They usually have much larger masses, velocity dispersions, and fractions of dense gas than molecular clouds that form early B or late O stars. This is compatible with earlier findings that more massive stars form in more massive cores. The IR luminosity-to-mass ratio has a mean value of $9 L_{\odot}/M_{\odot}$ and is little correlated with the cloud mass. Most molecular clouds have star formation efficiencies (SFE's) of 1%–2%. We find size-linewidth and size-density relations in the forms of $\Delta v \propto D^{0.4}$ and $n(\text{H}_2) \propto D^{-1.2}$. ^{13}CO cores are in general associated with compact HII regions regardless of the presence of UC HII regions therein. In contrast, CS cores are preferentially associated with compact HII regions that contain UC HII regions. As with the fact that the compact HII regions containing UC HII regions are more compact than those not associated with UC HII regions, these indicate that the former may be in an earlier evolutionary phase than the latter. The diffuse extended envelopes of HII regions often develop in the direction of decreasing molecular gas density. Based on detailed comparison of molecular line data with radio continuum and recombination line data, the extended ionized envelopes are likely the results of champagne flows in at least 10 sources in our sample. Together these results appear to support a published suggestion that the extended emission around UC HII regions can be naturally understood by combining the champagne flow model with the hierarchical structure of molecular clouds, taking into account various inclinations and low resolutions of our data. Additionally the blister model seems to be still applicable to most HII regions, even though massive stars usually form in the interiors rather than on the surfaces of molecular clouds. It is possible because massive star-forming clouds have hierarchical structure and irregular morphology.

Subject headings: HII regions— ISM: clouds— ISM: molecules — radio lines: ISM— stars: formation

¹Department of Astronomy, University of Illinois, 1002 West Green Street, Urbana, IL 61801; ktkim@astro.uiuc.edu

²Astronomy Program, SEES, Seoul National University, Seoul 151-742, Korea; koo@astrohi.snu.ac.kr

1. Introduction

Ultracompact (UC) HII regions are very small ($D \lesssim 0.1$ pc), dense ($n_e > 10^4$ cm $^{-3}$), and bright ($EM > 10^6$ pc cm $^{-6}$) photoionized gas regions (Wood & Churchwell 1989a; Kurtz, Churchwell, & Wood 1994). They are thought to represent an early stage of massive-star evolution, such that the newly formed stars are still embedded in their natal molecular clouds. Recently, however, it has been found that most UC HII regions are not isolated but surrounded by diffuse extended emission (Koo et al. 1996; Kim & Koo 1996, 2001; Kurtz et al. 1999). In Kim & Koo (2001, hereafter Paper I), we did a radio continuum and radio recombination line (RRL) survey towards 16 UC HII regions with simple morphology and large ratios of single-dish to VLA fluxes, and detected extended emission towards all the sources. The extended emission consists of one to several compact ($\sim 1'$ or 0.5–5 pc) components and diffuse extended ($2'–12'$ or 4–19 pc) envelope. All the UC HII regions but 2 spherical ones are located in the compact components, where they always correspond to the peaks of their associated compact components. (This positional coincidence we refer to as ‘the compact components with UC HII regions’ or ‘the compact HII regions with UC HII regions’ throughout this paper.) Moreover, the compact components with UC HII regions are smaller and denser than those without UC HII regions. Based on these morphological relations and RRL observations, it seems certain that the ultracompact, compact, and extended components in each source are physically associated, and it is likely that they are excited by the same ionizing source. Thus almost all (14/16) the UC HII regions may not be bona-fide ionization-bounded ‘UC HII regions’ but rather ultracompact cores of more extended HII regions. A simple statistical analysis of single-dish to VLA flux ratios further suggested that most UC HII regions previously known are associated with extended emission like our sources. Therefore, it is necessary to explain how the ultracompact, compact, and extended components, which have very different dynamical time scales, can coexist.

In Paper I, we proposed a model in which the coexistence of the three components can be easily explained by combining the champagne flow model with the hierarchical structure of molecular clouds. Recent high-resolution molecular line observations of massive star-forming regions revealed molecular clumps (~ 1 pc) and hot cores ($\lesssim 0.1$ pc) therein (see Kurtz et al. 2000 and references therein). The hot cores are likely to be the sites of massive star formation. An interesting feature is that typical sizes of the hot cores and molecular clumps are, respectively, in rough agreement with those of UC HII regions and their associated compact components. Our model suggested, on the basis of these results, that when an O star formed off-center within a hot core embedded in a molecular clump, the HII region would continue to be ultracompact inside the hot core for a long ($> 10^5$ yr) time while it grows to a few 1 pc outside the hot core. In the light of the model, the coexistence of ultracompact, compact, and extended components does not seem to be unusual for HII regions that expand in hierarchically clumpy molecular clouds, and the ultracompact and compact components would disappear one by one when the host hot core and then molecular clump are destroyed by the exciting star(s). In the past decade a number of groups have undertaken studies on hot cores and molecular clumps associated with UC HII regions (e.g., Cesaroni et al. 1994; Garay

& Rodríguez 1990). However, there has been no holistic study of the relationship between the three components of HII regions and their molecular gas counterparts.

In this study, we made ^{13}CO , CS, and C^{34}S line observations of molecular clouds associated with the 16 UC HII regions with extended envelopes in Paper I. The main scientific goals of our observations are (1) to explore the physical characteristics of the molecular clouds undergoing active massive star formation, (2) to investigate how the HII region complexes interact with their parental molecular clouds on diverse length scales, and (3) to understand the origin of the extended envelopes of UC HII regions. The observational details are described in § 2 and the results are presented in § 3. We discuss the physical properties and star formation of the molecular clouds, the interaction between the ionized and molecular gas, the origin of the extended halos of UC HII regions, and the implication of our results for the blister model of HII regions in § 4. Some individual sources are discussed in § 5. We conclude with a summary of our main results in the last section.

2. Observations

2.1. ^{13}CO J=1–0 Line

We have carried out ^{13}CO J=1–0 (110.20135 GHz) line observations of molecular clouds associated with the 16 UC HII regions studied in Paper I using the 12 m telescope of the National Radio Astronomy Observatory³ (NRAO) at Kitt Peak in 1997 June. The telescope has a full width at half-maximum (FWHM) of $60''$ at 110 GHz. The spectrometer used is a 256 channel filterbank with 64 MHz bandwidth providing a velocity resolution of 0.68 km s^{-1} . The system temperature was in the range 250–350 K. All the molecular clouds were mapped with $20''$ spacing using the “on-the-fly” observing technique. We used positions with some emission as reference positions, since we could not find any positions devoid of ^{13}CO emission near the sources. We obtained a sensitive spectrum of each reference position and added it to the position-switched spectra. The observed temperature (T_{R}^*) was converted to main-beam brightness temperature (T_{b}) using the corrected main-beam efficiency (0.84) provided by the NRAO. Table 1 shows the observational parameters.

2.2. CS and C^{34}S Line

We have conducted CS J=2–1 (97.98095 GHz) line observations of the molecular clouds in three observational runs from 1996 November to 1997 April. Ten sources were mapped with $60''$ spacing. In the remaining sources CS J=2–1 emission was usually detected only at the positions of the UC HII regions. We have also observed CS J=3–2 (146.96904 GHz), C^{34}S J=2–1

³The National Radio Astronomy Observatory is operated by Associated Universities, Inc., under cooperative agreement with the National Science Foundation

(96.41298 GHz), and C³⁴S J=3–2 (144.61711 GHz) emission towards the UC HII regions in 2000 March. The observations were made with the 14 m telescope of the Taeduk Radio Astronomy Observatory (TRAO), FWHMs of which are 60'' at 98 GHz and 46'' at 147 GHz. The line intensity was obtained on the T_A^* scale from chopper-wheel calibration. The telescope has main beam efficiencies of 0.48 (98 GHz) and 0.39 (147 GHz). All observations were made in the position switching mode with reference positions checked to be free from appreciable CS emission (Table 3). We used SIS mixer receivers with 256 channel filterbanks of 64 MHz bandwidth as the backend. The velocity resolutions were 0.77 km s⁻¹ and 0.51 km s⁻¹ at 98 GHz and 147 GHz, respectively. The system temperatures were typically 400K at 98 GHz and 700 K at 147 GHz.

3. Results

3.1. ¹³CO J=1–0 Line Results

Figures 1*a*–1*p* show our ¹³CO spectra, along with CS and C³⁴S spectra, at the positions of all the 16 UC HII regions. There are in general two or more velocity components in the line of sight, since the sources are located in the inner Galactic plane. In each source, however, it is not difficult to find the velocity component associated with H76α RRL emission, the center velocity of which is depicted by the vertical dotted line (Paper I). The H76α line is significantly ($\gtrsim 5$ km s⁻¹) shifted from the associated ¹³CO line in 6 sources: G5.97–1.17, G10.15–0.34, G10.30–0.15, G12.21–0.10, G23.71+0.17, and G27.28+0.15. The mean difference between the two velocities is 3.2 ± 3.2 km s⁻¹ for all the sources but G12.43–0.05 where H76α line emission was not detected. A similar result was obtained by Forster et al. (1990), who observed two hydrogen RRLs and seven molecular lines towards 9 compact HII regions and found velocity differences of typically 6 km s⁻¹. Thus such a velocity difference between the ionized and molecular gas seems to be a common feature. The velocity offset can be attributed to bulk motion of the ionized gas as the HII region expands asymmetrically in the direction of decreasing molecular density, as suggested by Forster et al. (1990).

Figures 2*a*–2*o* exhibit integrated ¹³CO line intensity maps of molecular clouds. The integrated velocity range is given at the top in each panel. The UC HII regions and strong compact HII regions are, respectively, marked by large and small crosses in the individual panels (see Table 3 of Paper I). The maps well reveal clumpy structure and irregular morphology of molecular clouds, especially for clouds at relatively small distances, such as G5.89–0.39, G5.97–1.17, G8.14+0.23, G10.15–0.34, and G10.30–0.15. The typical size of clumps is $\sim 1'$. The UC and compact HII regions are usually associated with dense cores in the molecular clouds. The individual sources will be discussed in some detail in § 5.

If molecular gas is in local thermodynamical equilibrium (LTE), the optical depth of ¹³CO J=1–0 line can be calculated from the observed intensity as compared with the excitation temperature which is assumed to be equal to the observed ¹²CO brightness temperature. In that case the

^{13}CO column density is given by the relation

$$N(^{13}\text{CO}) = 2.42 \times 10^{14} \frac{T_{\text{ex}} \int \tau^{13} dv}{1 - \exp(-5.29/T_{\text{ex}})} \quad (\text{cm}^{-2}), \quad (1)$$

where T_{ex} is the excitation temperature in K, τ^{13} is the optical depth, and v is the velocity in km s^{-1} . We estimated the masses of molecular clouds, M_{LTE} , using the distances given by Wood & Churchwell (1989) (Table 1) and the ^{12}CO brightness temperatures obtained from the Massachusetts-Stony Brook Galactic Plane Survey (Sanders et al. 1986). It was assumed in this calculation that the mean molecular weight is $2.3 m_{\text{H}}$ and the ratio of $N(^{13}\text{CO})/N(\text{H}_2)$ is 2×10^{-6} (Dickman 1978).

Table 2 lists the physical parameters of molecular clouds, such as geometric mean radius R , M_{LTE} , H_2 molecule number density $n(\text{H}_2)$, and FWHM of the average spectrum of cloud Δv . The molecular clouds have sizes of 7–48 pc, masses of $(1-102) \times 10^4 M_{\odot}$, densities of $(1.6-10.3) \times 10^2 \text{ cm}^{-3}$, and line widths (FWHMs) of 4.1–10.2 km s^{-1} .

3.2. CS and C^{34}S Line Results

We detected CS J=2–1 emission in all sources observed (Fig. 1). The center velocity of CS gas is in good agreement with that of ^{13}CO gas. Unlike ^{13}CO emission, there is a single velocity component in CS line emission along the line of sight for all the sources with one exception (G23.46–0.20) and it is always associated with the UC HII region (see also Fig. 3). Towards G23.46–0.20, a velocity component with $v_{\text{LSR}} \simeq 100 \text{ km s}^{-1}$ was observed over the entire area mapped (Figs. 1*i* & 3*g*) and an additional component was detected at about 80 km s^{-1} in the southern dense core. For the determination of the CS column density, $N(\text{CS})$, we used the following formula

$$N(\text{CS}) = 1.88 \times 10^{11} T_{\text{r}} \exp(7.05/T_{\text{r}}) \int T_{\text{b}} dv \quad (\text{cm}^{-2}), \quad (2)$$

which is valid for the optically thin case. Here T_{r} is the rotation temperature in K, T_{b} is the brightness temperature in K, and v is the velocity in km s^{-1} . We assumed T_{r} to be 30 K based on studies of dense molecular gas in massive star-forming regions (see, e.g., Snell et al. 1984; Linke & Goldsmith 1980; Churchwell et al. 1990). The $N(\text{H}_2)$ was derived from $N(\text{CS})$ using a fractional CS abundance to H_2 of 1×10^{-9} (Linke & Goldsmith 1980; Frerking et al. 1980). Table 3 presents CS J=2–1 line parameters and $N(\text{CS})$ at the positions of UC HII regions.

We also detected CS J=3–2 emission in all the UC HII regions but one (G12.43–0.05), and C^{34}S J=2–1 and J=3–2 emission in several sources (Tables 3 & 4). The optical depth of C^{34}S emission, τ_{p} , can be computed from the peak brightness temperature ratio by assuming that the excitation temperature and the beam filling factor are identical in the CS and C^{34}S lines in each transition, using the formula

$$T_b(\text{C}^{34}\text{S})/T_b(\text{CS}) = [1 - \exp(-\tau_p)]/[1 - \exp(-\tau_p r)]. \quad (3)$$

Here r is the CS to C^{34}S abundance ratio, which we assumed to be equal to the terrestrial value (22.5). The estimated τ_p and C^{34}S line parameters are summarized in Table 4.

Figure 3a – 3j show CS J=2–1 integrated intensity maps of the 10 sources mapped. CS-emitting regions are fairly clumpy and of irregular morphology. The UC HII regions are nearly always associated with the strongest CS cores in the individual sources (see § 4.2). We determined the physical parameters of the CS-emitting regions, including R , M_{LTE} , $n(\text{H}_2)$, and Δv (Table 5). The CS-emitting regions have sizes of 3–27 pc, masses of $(3\text{--}470)\times 10^3 M_\odot$, densities of $(0.9\text{--}5.9)\times 10^3 \text{ cm}^{-3}$, and line widths (FWHMs) of 3.4–10.0 km s^{-1} .

3.3. Correlation among Physical Parameters

Similar power-law correlations were found between D and Δv and between D and $n(\text{H}_2)$ both for one line from cloud to cloud and for various lines of a cloud. This suggests that a widespread and fundamental process operates in molecular clouds. Figure 4 is a plot of Δv against D for the molecular clouds in our sample. A fairly good correlation exists between the two parameters. Here open circles are data points derived from ^{13}CO data, whereas filled circles are the ones measured using CS data. We performed a least-squares fit to the data points and obtained $\log \Delta v = (0.35\pm 0.06) \log D + 0.4\pm 0.1$ with a linear correlation coefficient of 0.80. Figure 5 displays $n(\text{H}_2)$ versus D . There is also a strong correlation between the two. A least-squares fit yields $\log n(\text{H}_2) = (-1.24\pm 0.15) \log D + 4.4\pm 0.2$ with a correlation coefficient of -0.86 . The estimated slopes of the two relations are in reasonable agreement with the values determined for large samples of molecular clouds and dense cores in the Galaxy. For example, Larson (1981) obtained $n(\text{H}_2) \propto D^{-1.1}$ and $\Delta v \propto D^{0.38}$ relationships for about 50 molecular complexes, clouds, and clumps. Myers (1983) and Dame et al. (1986) also found similar power-law relations for smaller clouds and cores and for larger complexes, respectively. Several explanations were proposed to understand these relations but it is beyond the scope of this paper to mention them in detail (see, e.g., Myers & Goodman 1988). In Paper I we found a relation between electron density and size of the form $n_e \propto D^{-1.0}$ for HII regions in our sample, and proposed that the relation reflects variation in the ambient molecular gas density. The observed D - $n(\text{H}_2)$ relationship with a similar power-law index for the host clouds and cores might be direct evidence supporting the idea.

4. Discussion

4.1. Physical Characteristics and Star Formation

The molecular clouds in our sample are associated with extended radio HII regions, each of which consists of an UC HII region, compact component(s), and diffuse extended envelope. As mentioned in § 1, the UC HII regions and their associated compact components are likely to be ionized by the same sources. In case where there are two or more compact components, e.g., G29.96–0.02 (Fig. 8*m*), the compact components may be produced by separate ionizing sources (Paper I). Assuming that the compact components are excited by single zero-age main-sequence stars, their ionizing sources are O7 to O4 stars (see Table 4 of Paper I). If a stellar cluster is responsible for the ionization, alternatively, the most massive star in the cluster would be about two subclasses later than the equivalent single-star spectral type (cf. Kurtz et al. 1994). In either case the observed molecular clouds seem to be the ones that give birth to very massive stars.

We compare the physical properties of our molecular clouds with those of molecular clouds with some indicators of massive star formation. Some groups made CO and ^{13}CO J=1–0 line observations of nearby molecular clouds associated with Sharpless HII regions (Carpenter, Snell, & Schloerb 1995a; Heyer, Carpenter, & Ladd 1996). These molecular clouds appear to form lower-mass stars than our molecular clouds, since the associated HII regions are usually excited by early B or late O stars. They have sizes of 10–50 pc, masses of $(1-7)\times 10^4 M_{\odot}$, and line widths (FWHMs) of 2–6 km s $^{-1}$. Despite similar sizes the molecular clouds in our sample have considerably larger masses and velocity dispersions. Such molecular clouds were also studied in CS J=2–1 line emission (Zinchenko et al. 1994; Carpenter, Snell, & Schloerb 1995b). Their CS-emitting regions have sizes of 1–5 pc, masses of $(1-140)\times 10^2 M_{\odot}$, and line widths (FWHMs) of 2–3 km s $^{-1}$. The CS-emitting regions of our molecular clouds are significantly larger, more massive, and more turbulent. In Table 5 we give the estimated fraction of the CS-emitting region to the whole cloud in mass and area of our sample. The CS-emitting regions on average contain $45\pm 18\%$ of the total mass and occupy $20\pm 8\%$ of the total area. The measured fractions are much higher than estimates for the nearby molecular clouds with Sharpless HII regions. For example, the mass and area fractions are, respectively, 2% and 1% for the Gemini OB1 cloud complex that contains several Sharpless HII regions (Carpenter et al. 1995b). This result is compatible with the finding of Carpenter et al. (1995b) that more luminous *IRAS* sources are in general associated with more massive CS cores in the Gemini complex, which strongly implies that more massive stars form in more massive cores. Similar trends have been observed in the L1630 molecular cloud (Lada 1992) and the Rosette molecular cloud (Phelps & Lada 1997) as well. In these molecular clouds the embedded clusters are associated with the most massive cores. Thus it was suggested that both high gas density and high gas mass are required for the formation of stellar clusters. In view of this, it is not surprising that our molecular clouds, which form rich stellar clusters and/or very massive single stars, have very massive CS cores.

The ratio of infrared (IR) luminosity to mass is a good measure of the massive star formation

activity of molecular clouds. We derive the ratio for the molecular clouds in our sample using *IRAS* HIgh RESolution processing (HIRES) images. The total IR luminosity between 1 μm and 500 μm , L_{IR} , can be estimated from the 60 μm and 100 μm flux densities in Jy, F_{60} and F_{100} , by the relation (Lonsdale et al. 1985; Lee et al. 1996)

$$L_{\text{IR}} = 0.394 R(\overline{T_d}, \beta) [F_{100} + 2.58 F_{60}] d^2 \quad (L_{\odot}). \quad (4)$$

Here T_d is the 60/100 μm color temperature in K, β is the index in the emissivity law, $Q_{\text{abs}} \sim \lambda^{-\beta}$, and d is the source distance in kpc. The $R(\overline{T_d}, \beta)$ is the color correction factor that accounts for the flux radiated outside the 60 μm and 100 μm *IRAS* bands. Table 6 lists L_{IR} and $L_{\text{IR}}/M_{\text{LTE}}$ for the individual sources. In this calculation β was assumed to be 1 (Hildebrand 1983). The ratio $L_{\text{IR}}/M_{\text{LTE}}$ has a mean value of $9.1 \pm 6.0 L_{\odot}/M_{\odot}$, which is much greater than the average ratio ($2.8 L_{\odot}/M_{\odot}$) of all molecular clouds in the inner Galactic plane but is comparable to the median value ($7 L_{\odot}/M_{\odot}$) for molecular cloud complexes with HII regions (Scoville & Good 1989). Figure 6 compares the ratio with M_{LTE} . There does not seem to be any apparent correlation between the two parameters. This matches with the results of Mooney & Solomon (1988), Scoville & Good (1989), and Carpenter, Snell, & Schloerb (1990), who found no correlation over the mass range $10^2 - 10^7 M_{\odot}$.

We examine the relationship between stellar mass, M_* , and cloud mass, as shown in the lower panel of Figure 7. In this comparison M_* 's were derived from the Lyman continuum photon fluxes, N'_c 's, measured by Paper I using $\langle M_* \rangle / \langle N'_c \rangle = 5.7 \times 10^{-47} M_{\odot} (\text{photons s}^{-1})^{-1}$ (McKee & Williams 1997; see also Mezger, Smith, & Churchwell 1974). We performed a least-squares fit to all the data points and obtained $\log M_* = (0.62 \pm 0.12) \log M_{\text{LTE}} + 0.1 \pm 0.6$ with a correlation coefficient of 0.83. The slope agrees within errors with that (0.5 ± 0.2) found by Myers et al. (1986) for a sample of 54 molecular cloud complexes in the inner Galaxy. We determine star formation efficiencies (SFE's), $M_*/(M_* + M_{\text{cloud}})$ (Table 6). Most clouds in our sample have SFE's comparable to the Galactic median value of 1%–2% (Myers et al. 1986; Leisawitz, Bash, & Thaddeus 1989), while G5.97–1.17 and G37.55–0.11 have very high SFE's (>5%). They would have been classified as the most efficient star-forming clouds by Myers et al. (1986), who found only 4 molecular clouds with SFE's $\geq 4\%$ (M16, M17, W49, and W51) in their sample (cf. Koo 1999). Since they are the clouds with the least masses, however, the high SFE's can be due to the disruption of molecular gas by massive stars. This appears to be true for G5.97–1.17 (see § 5.2). If the two clouds are excluded, a least-squares fit yields $\log M_* = (0.86 \pm 0.12) \log M_{\text{LTE}} - 1.3 \pm 0.7$ with a higher (0.90) correlation coefficient, so that the slope appears to be fairly steeper than the former. The value of SFE has little correlation with M_{LTE} , as might be expected from the independence of $L_{\text{IR}}/M_{\text{LTE}}$ on M_{LTE} .

4.2. Interaction between Ionized and Molecular Gas

Figures 8*a*–8*o* compare the distribution of ionized gas with that of molecular gas in our sources. The extended envelopes of HII regions seem to be largely determined by the ambient molecular gas distribution, since they often develop in the direction of decreasing molecular gas density. G8.14+0.23 and G10.30–0.15 provide good examples. In these sources, the central compact components are associated with ^{13}CO cores, while the diffuse envelopes stretch out oppositely along the axes approximately orthogonal to the elongated natal molecular clouds. Such a bipolar morphology is very reminiscent of champagne flows that would arise from a flat molecular cloud (Bodenheimer, Tenorio-Tagle, & Yorke 1979; Tenorio-Tagle, Yorke, & Bodenheimer 1979). The large velocity gradients expected in the champagne flows were not observed in these objects, however, although they could be present but masked by large inclination angles. We have found using the H76 α line data in 7 sources (G5.89–0.39, G5.97–1.17, G10.15–0.34, G10.30–0.15, G12.21–0.10, G23.46–0.20, and G29.96–0.02) that the extended envelopes are blue- or red-shifted by 3–10 km s $^{-1}$ from the UC HII regions (Paper I). The H76 α line is considerably shifted with respect to molecular lines in several sources, as noted in § 3.1. Based on the morphological comparison between HII regions and molecular clouds, the velocity gradient in H76 α line emission, and the velocity difference between H76 α and molecular lines, the extended envelopes can be interpreted as consequences of champagne flows in at least 10 sources in our sample: G5.97–1.17, G8.14+0.23, G10.15–0.34, G10.30–0.15, G12.21–0.10, G12.43–0.05, G23.46–0.23, G23.71+0.17, G23.96+0.15, and G27.28+0.15 (Israel 1978; Tenorio-Tagle 1979; Franco, Tenorio-Tagle, & Bodenheimer 1990). It should be noted that an obvious anti-correlation between the distributions of the ionized and molecular gas cannot be seen unless the inclination of the champagne flow is large, and that low resolution and coarse sampling of our RRL observations prevent us from examining the internal velocity gradient of the ionized gas in the majority of our sources. The results of this inspection on the individual sources will be discussed in § 5.

We investigate the association between compact HII regions and ^{13}CO cores from Figure 8. The vast majority of compact HII regions are associated with ^{13}CO cores, which are in general the densest ones in the individual sources. However, the radio continuum peaks and their associated ^{13}CO peaks usually do not overlap. This is more clearly shown in Figure 9, which is a histogram demonstrating the number of compact HII regions at each separation interval between the peaks of radio continuum and ^{13}CO intensities. Figure 9 also displays that there may be no significant difference in statistics between the compact HII regions with and without UC HII regions. We performed a similar analysis for CS cores as well. All the compact HII regions with UC HII regions are intimately related to CS peaks, whereas those without UC HII regions are mainly shifted from the peaks (see, e.g., Figs. 3*d* & 3*f*). CS gas was detected only at the positions of UC HII regions in the sources not mapped, as said earlier. We did not analyze statistically the separation of the radio continuum peaks and the associated CS peaks, because the sampling interval (60'') of our CS line maps is comparable to or larger than the typical angular separation between the two peaks.

4.3. Origin of Extended Emission around UC HII regions

In Paper I we suggested a simple model to explain the origin of the extended envelopes of UC HII regions (see also § 1). In the model the extended envelopes are produced by champagne flows originating from hot cores of molecular clouds. However, we could not completely exclude the possibility that they are formed during the initial ionization of HII regions. This is possible if hot cores and molecular clumps are so clumpy that ultraviolet (UV) photons can propagate a few 1 pc from the central stars. How can we distinguish between the two possibilities? For doing this it seems to be important to compare in detail the ionized gas distribution in the envelopes with the ambient molecular gas distribution. The extended envelopes are expected to stretch out in the direction of decreasing molecular gas density in both cases. If they were formed very soon after the central stars turned on, the density distribution of ionized gas would be very similar to that of molecular gas because it is not yet significantly affected by dynamical evolution. On the contrary, the two density distributions could be substantially different each other if the extended envelopes were formed by champagne flows. In this context, our data appear to support the champagne flow model. In G8.14+0.23 at a distance of 4.2 kpc, for example, the ionized gas protuberances extend into molecular gas hollows that lie north and south of the central dense core (Fig. 8*d*). We can also see similar features in other sources at relatively small ($d \leq 6$ kpc) distances, such as the eastern part of G10.15–0.34 and the northern part of G10.30–0.15 (Fig. 8*e*). In particular, a velocity variation of ~ 10 km s⁻¹ was actually observed along $\delta(1950) \simeq -20^\circ 20' 05''$ in the extended envelope of G10.15–0.34 (Kim & Koo 2002). There is sometimes a significant velocity difference between the RRL and molecular line emission observed towards each UC HII region. The RRL width is generally larger in the compact HII regions, especially the ones with UC HII regions, than in the extended envelopes (Paper I; Garay & Rodríguez 1983). These might be also strong arguments in favor of the champagne flow model, even though detailed comparison of radio continuum and RRL data with molecular line data at a higher resolution is needed to clarify this issue.

We found in Paper I that the compact HII regions with UC HII regions are smaller and denser than those without UC HII regions, and proposed that the former might be in an earlier evolutionary phase than the latter. Since massive stars emit strong UV radiation, stellar winds, and energetic bipolar outflows even at the earliest evolutionary stage, the host dense cores should be disrupted with time. Thus our suggestion matches with that the compact HII regions with UC HII regions are more closely associated with CS peaks than those without UC HII regions. These observations are consistent with our model. On the other hand, two spherical UC HII regions in our sample, G23.46–0.23 and G25.72+0.05, have no associated compact HII regions (Figs. 8*h* & 8*k*). G25.72+0.02 is coincident with a ¹³CO core and has detectable CS emission only at the UC HII region position, but G23.46–0.20 is significantly offset from the nearby ¹³CO and CS peaks (Figs. 2*h* & 3*g*). The absence of associated dense core and compact HII region indicates that G23.46–0.23 may be an externally ionized dense clump. In contrast, G25.72+0.05 is likely to be the only bona-fide ionization-bounded UC HII region out of the 16 UC HII regions in our sample.

4.4. Revisit to Blister Model of HII regions

Zuckerman (1973) for the first time suggested that the Orion Nebula is a blister-like HII region located on the near edge of an associated molecular cloud. After that Israel (1978) found from a comparison of optical HII regions and molecular clouds that the majority of HII regions in his sample have similar structures to the Orion nebula and further proposed that the formation of massive stars occur near the surfaces of molecular clouds (see also Israel 1976, 1977). Subsequent numerical simulations successfully demonstrated that such a blister-like morphology of HII regions can be produced by champagne flows derived by density contrast between molecular clouds and intercloud medium and/or strong negative density gradient in molecular clouds (e.g., Tenorio-Tagle 1979; Franco et al. 1990). However, Waller et al. (1987) showed by comparing radio HII regions and molecular clouds that radio HII regions are preferentially concentrated toward the centers of molecular clouds, and argued that the result conflicts with the blister picture.

On the other hand, our data show that the compact (and ultracompact) components of HII regions are closely associated with dense cores of molecular clouds. Since most of the dense cores are deeply embedded in molecular clouds, it is likely that massive stars in general form in the interiors rather than on the surfaces of molecular clouds. This is consistent with what Waller et al. (1987) found. However, our data strongly suggest that the diffuse extended envelopes of HII regions are produced by champagne flows. Thus the blister picture appears to be still applicable to most HII regions. It seems possible because massive star-forming molecular clouds have hierarchical structure and are of irregular morphology. In view of our model, the peaks of optical HII regions are likely to be located around the edges of associated molecular clouds not because the exciting star(s) formed there, but because the side of the molecular cloud had already been disrupted by champagne flows.

5. Comments on Some Individual Sources

5.1. G5.89–0.39

This molecular cloud provides a good example showing that the molecular clouds in our sample are very clumpy and of irregular morphology (Fig. 2a). The molecular cloud is moderately elongated in the northwest-southeast direction on the whole and is largely divided into three components: central, northwestern, and southeastern ones. Apparently massive star formation is ongoing only in the central component. The central component has two dense cores, which are associated with the strong compact components in the radio continuum (Fig. 8a). The UC HII region is located in the western denser core, which is consistent with the idea that the compact components with UC HII regions are in an earlier evolutionary stage than those without UC HII regions.

5.2. G5.97–1.17

Among our sources this is the nearest (1.9 kpc) one and so the molecular cloud reveals very well the clumpy structure (Fig. 2*b*). The cloud is composed of an extended ($\sim 6' \times 10'$) component and an arclike structure, which emanates from the former to the southeast. The arclike structure has radio continuum counterpart (Fig. 8*b*). The UC HII region is associated with a weak dense core, which resides at the edge of the central component. The strongest ^{13}CO core is located northwest of the cloud but shows no indication of ongoing massive star formation in radio and mid-infrared continuum emission (Crowther & Conti 2003). As pointed out in Paper I, our extended radio HII region is the dense part of the well-known Lagoon nebula (M8). It seems that the dense part is ionized mainly by Herschel 36 (O7), nearly corresponding to the UC HII region in position, while more extended optical nebulosity is excited by other O stars, including 9 Sgr (O4(f)) (Elliot et al. 1984). The ionized gas is significantly ($>5 \text{ km s}^{-1}$) blue-shifted from the molecular gas (Fig. 1*b* and Table 5 of Paper I), which indicates that the HII region is on the front edge of the host molecular cloud and the ionized gas is approaching the Earth with respect to the molecular cloud, as proposed by Lada et al. (1976). The star 9 Sgr is located about $3'$ east of UC HII region, i.e., $(\alpha, \delta)_{1950} = (18^{\text{h}}00^{\text{m}}49^{\text{s}}.8, -24^{\circ}22'00'')$. Thus the eastern hollow may have been produced by strong UV radiation and stellar winds from the star 9 Sgr. Consequently, the molecular cloud seems to have been considerably disrupted by O stars therein. This is compatible with the fact that the molecular cloud has a much higher SFE, 7.0%, in comparison with other clouds in our sample (Table 6).

5.3. G8.14+0.23

The molecular cloud is largely extended in the northeast-southwest direction, but the central dense part is elongated in the east-west direction (Figs 2*d* & 3*c*). The UC HII region is placed in the flattened dense core, a little west of the peak, which strongly supports that the bipolar morphology of HII region is the result of champagne flows originating from a thin molecular cloud (see § 4.2). In the view of the model presented in Paper I, this object is a good example of bipolar blister-type HII regions observed at a viewing angle close to 90° .

5.4. G10.15–0.34 and G10.30–0.15

This region is known as the W31 HII region/molecular cloud complex. The molecular cloud seems to be an incomplete shell, being open to the northwest, on the whole (Fig. 2*e*). The two UC HII regions are located in the southern spherical dense region and in the northern flat one, respectively. We found convincing observational evidence that their extended ionized envelopes have been produced by champagne flows (e.g., see Fig. 8*e*). A detailed radio and infrared study on this region was presented in a separate paper (Kim & Koo 2002).

5.5. G12.43–0.05

The UC HII region is situated outside the ^{13}CO core, although it has an associated compact component in the radio continuum (Fig. 8g). We have detected weak ($T_{\text{A}}^* \simeq 0.3$ K) CS J=2–1 line emission only at the position of the UC HII region (Fig. 1h). The associated compact component is the largest and most diffuse among the 14 compact components with UC HII regions in our sample (see Tables 3 & 4 of Paper I). In the picture of our model, it may suggest that the natal hot core has been almost destroyed by the ionizing star(s). Thus the compact component is likely on the verge of being one without ultracompact core.

5.6. G23.46–0.20

G23.46–0.20 is one of the two spherical UC HII regions that have no associated compact components in the radio continuum images. It is located near the boundary of extended envelope (Fig. 8h). There are no associated ^{13}CO or CS cores as well (Figs. 2h & 3g). Therefore, G23.46–0.20 might be a dense clump externally ionized by nearby luminous stars. The molecular cloud is roughly extended in the northwest-southeast direction, while the diffuse envelope of HII region is elongated in the east-west direction. According to RRL data obtained in Paper I, the northern and western parts are blue-shifted by ~ 4 km s $^{-1}$ from the central region, which has approximately the same (~ 104 km s $^{-1}$) center velocity as the molecular gas (Fig. 1i). These observations may indicate that the extended envelope is the result of champagne flows.

5.7. G23.71+0.17

The UC HII region corresponds to the peak of an extended HII region whose compact component is associated with a ^{13}CO core (Fig 8i). CS J=2–1 and J=3–2 emission were detected only towards the UC HII region (Table 3). The H76 α line (103.0 km s $^{-1}$) is blueshifted from the ^{13}CO and CS lines by about 12 km s $^{-1}$ (Fig 1j), suggesting that the HII region may be located on the near edge of the molecular cloud. The situation is very similar to G5.17–1.17 (§ 5.2) or the Orion nebula (Zuckerman 1973), even if this object is at a much larger (9 kpc) distance. The viewing angle does not seem to be very small because the diffuse envelope of the HII region is more extended to the northeast.

5.8. G23.96+0.15 and G27.28+0.15

These two UC HII regions are located in ^{13}CO and CS cores. The molecular clouds are elongated in the north-south direction, while the diffuse envelopes of HII regions fairly extended in the perpendicular direction (Figs 8j & 8l). Thus the extended envelopes can be interpreted

as champagne flows. However, we could not observe any internal velocity gradient due to low (FWHM $\simeq 2'$) angular resolution of RRL observations.

5.9. G29.96–0.02

The UC HII region is associated with a local ^{13}CO peak, whereas it is located in the strongest CS peak (Figs 2*m* & 3*j*). The dense region of the molecular cloud is somewhat elongated in the northeast-southwest direction. In the channel maps of both ^{13}CO and CS line data, a significant ($\sim 8 \text{ km s}^{-1}$) velocity gradient is present. Strong ^{13}CO - and CS-emitting regions move from northeast to southwest as the velocity increases from $v_{\text{LSR}} \simeq 92 \text{ km s}^{-1}$ to 100 km s^{-1} . We can find a similar velocity gradient in the RRLs taken in approximately full-beam spacing along $\alpha(1950) \approx 18^{\text{h}}43^{\text{m}}28^{\text{s}}.0$ (see Table 5 of Paper I).

6. Conclusions

We carried out ^{13}CO J=1–0, CS, and C^{34}S J=2–1 and J=3–2 line observations of the parental molecular clouds of 16 UC HII regions with extended envelopes, which give rise to rich stellar clusters and/or very massive (O7–O4) stars. The molecular clouds in our sample are very clumpy and of irregular morphology. Our molecular clouds and dense cores usually have much larger masses and velocity dispersions than those associated with Sharpless HII regions that are ionized by early B or late O stars. The CS-emitting regions on average contain $\sim 45\%$ of the total cloud mass and occupy $\sim 20\%$ of the total area for the 10 sources mapped in the CS J=2–1 line. The estimated fractions are one order of magnitude higher than the values for the molecular clouds that form early B or late O stars. This result is consistent with the earlier findings for smaller dense cores that more massive stars form in more massive cores.

^{13}CO cores are in general associated with compact HII regions regardless of the presence of UC HII regions therein, while CS cores are preferentially associated with those with UC HII regions. Along with the fact that the compact HII regions with UC HII regions are more compact than those without UC HII regions, this strongly suggests that the former are in an earlier evolutionary stage than the latter. The extended envelopes of HII regions tend to develop towards molecular regions of low density. It was found in some sources at relatively small ($d \leq 6 \text{ kpc}$) distances that the density distribution of ionized gas in the envelopes is substantially different from that of the ambient molecular gas, indicating that the ionized gas distribution have been significantly affected by dynamical evolution. Thus it seems likely that the extended envelopes have been formed by champagne flows rather than the initial ionization, although higher-resolution radio continuum, molecular line, and especially RRL observations are required to clarify this issue. Based on the morphological comparison of HII regions and molecular clouds, the velocity gradient in H76 α line emission, and the velocity difference between H76 α and molecular lines, the extended ionized

envelopes are likely to be the consequences of champagne flows in at least 10 sources in our sample. Together, these results appear to support our model that explains the presence of low-density halos of UC HII regions by combining the champagne flow model with the hierarchical structure of molecular clouds, taking into account various inclinations and low resolutions of our data.

Our results do not imply, however, that the formation of massive stars takes place near the surfaces of molecular clouds as proposed by the original blister model of HII regions (Israel 1978). Instead, since the UC and compact components of HII regions mainly correspond to the dense cores embedded in molecular clouds, massive stars seem to form in the interiors of molecular clouds. Nevertheless, the diffuse extended envelopes of HII regions can be produced by champagne flows because massive star-forming molecular clouds have hierarchical structure and irregular morphology.

We are very grateful to Ed Churchwell, Stan Kurtz, and Guillermo Tenorio-Tagle for thoughtful comments and discussion. We also thank the anonymous referee for helpful suggestions and comments. This work has been supported by BK21 Program, Ministry of Education, Korea through SEES, and also the Laboratory for Astronomical Imaging at the University of Illinois and NSF grant AST 99-81363.

REFERENCES

- Bodenheimer, P., Tenorio-Tagle, G., & Yorke, H. W. 1979, *ApJ*, 233, 85
- Carpenter, J. M., Snell, R. L., & Schloerb, F. P. 1990, *ApJ*, 362, 147
- . 1995a, *ApJ*, 445, 246
- . 1995b, *ApJ*, 450, 201
- Cesaroni, R., Churchwell, E., Hofner, P., & Walmsley, C. M. 1994, *A&A*, 288, 903
- Churchwell, E., Walmsley, C. M., & Cesaroni, R. 1990, *A&AS*, 83, 119
- Crowther, P. A., & Conti, P. S. 2003, *MNRAS*, in press
- Dame, T. M., Elmegreen, B. G., Cohen, R. S., & Thaddeus, P. 1986, *ApJ*, 305, 892
- Dickman, R. L. 1978, *ApJS*, 37, 407
- Elliot, K. H., Goudis, C., Hippelein, H., & Meaburn, J. 1984, *A&A*, 138, 451
- Forster, J. R., Caswell, J. L., Okumura, S. K., Hasegawa, T., & Ishiguro, M. 1990, *A&A*, 231, 473
- Franco, J., Tenorio-Tagle, G., & Bodenheimer, P. 1990, *ApJ*, 349, 126
- Frerking, M. A., Wilson, R. W., Linke, R. A., & Wannier, P. G. 1980, *ApJ*, 240, 65
- Garay, G., & Rodríguez, L. 1983, *ApJ*, 266, 263
- Garay, G., & Rodríguez, L. 1990, *ApJ*, 362, 191
- Heyer, M. N., Carpenter, J. H., & Ladd, E. F. 1996, *ApJ*, 463, 630
- Israel, F. P. 1976, *A&A*, 48, 193
- . 1977, *A&A*, 59, 27
- . 1978, *A&A*, 70, 769
- Kim, K.-T., & Koo, B.-C. 1996, *J. Korean Astron. Soc.*, 29, S177
- . 2001, *ApJ*, 549, 979 (Paper I)
- . 2002, *ApJ*, 575, 327
- Koo, B.-C. 1999, *ApJ*, 518, 760
- Koo, B.-C., Kim, K.-T., Lee, H.-G., Yun, M.-S., & Ho, P. T. P. 1996, *ApJ*, 456, 662
- Kurtz, S., Cesaroni, R., Churchwell, E., Hofner, P., & Walmsley, C. M. 2000, in *Protostars and Planets IV*, ed. V. Mannings, A. Boss, & S. Russell (Tucson: Univ. Arizona Press), 299
- Kurtz, S., Churchwell, E., & Wood, D. O. S. 1994, *ApJS*, 91, 659
- Kurtz, S., Watson, A. M., Hofner, P., & Otte, B. 1999, *ApJ*, 514, 232
- Lada, C. J., Gull, T. R., Gottlieb, C. A., & Gottlieb, E. W. 1976, *ApJ*, 203, 159
- Lada, E. A. 1992, *ApJ*, 393, L25
- Larson, R. B. 1981, *MNRAS*, 194, 809

- Lee, Y., Snell, R. L., & Dickman, R. L. 1996, *ApJ*, 472, 275
- Leisawitz, D., Bash, F. N., & Thaddeus, P. 1989, *ApJS*, 70, 731
- Linke, R. A., & Goldsmith, P. F. 1980, *ApJ*, 235, 437
- Lonsdale, C. J., Helou, G., Good, J. C., & Rice, W. L. 1985, *Catalogued Galaxies and Quasars Observed in the IRAS Survey* (Washington, DC: GPO)
- McKee, C. F., & Williams, J. P. 1997, *ApJ*, 476, 144
- Mezger, P. G., Smith, L. F., & Churchwell, E. 1974, *A&A*, 32, 269
- Mooney, T. J., & Solomon, P. M. 1988, *ApJ*, 334, L51
- Myers, P. C. 1983, *ApJ*, 270, 105
- Myers, P. C., Dame, T. M., Thaddeus, P., Cohen, R. S., Silverberg, R. F., Dwek, E., & Hauser, M. G. 1986, *ApJ*, 301, 398
- Myers, P. C., & Goodman, A. A. 1988, *ApJ*, 329, 392
- Phelps, R. L., & Lada, E. A. 1997, *ApJ*, 477, 176
- Sanders, D. B., Clemens, D. B., Scoville, N. Z., & Solomon, P. M. 1986, *ApJS*, 60, 1
- Scoville, N. Z., & Good, J. C. 1989, *ApJ*, 339, 149
- Snell, R. L., Goldsmith, P. F., Erickson, N. R., Mundy, L. G., & Evans, N. J. II 1984, *ApJ*, 276, 625
- Tenorio-Tagle, G. 1979, *A&A*, 71, 59
- Tenorio-Tagle, G., Yorke, H. W., & Bodenheimer, P. 1979, *A&A*, 80, 110
- Waller, W. H., Clemens, D. P., Sanders, D. B., & Scoville, N. Z. 1987, *ApJ*, 314, 397
- Wood, D. O., & Churchwell, E. 1989a, *ApJS*, 69, 831
- . 1989b, *ApJ*, 340, 265
- Zinchenko, I., Forsström, V., Lapinov, A., & Mattila, K. 1994, *A&A*, 288, 601
- Zuckerman, B. 1973, *ApJ*, 183, 863

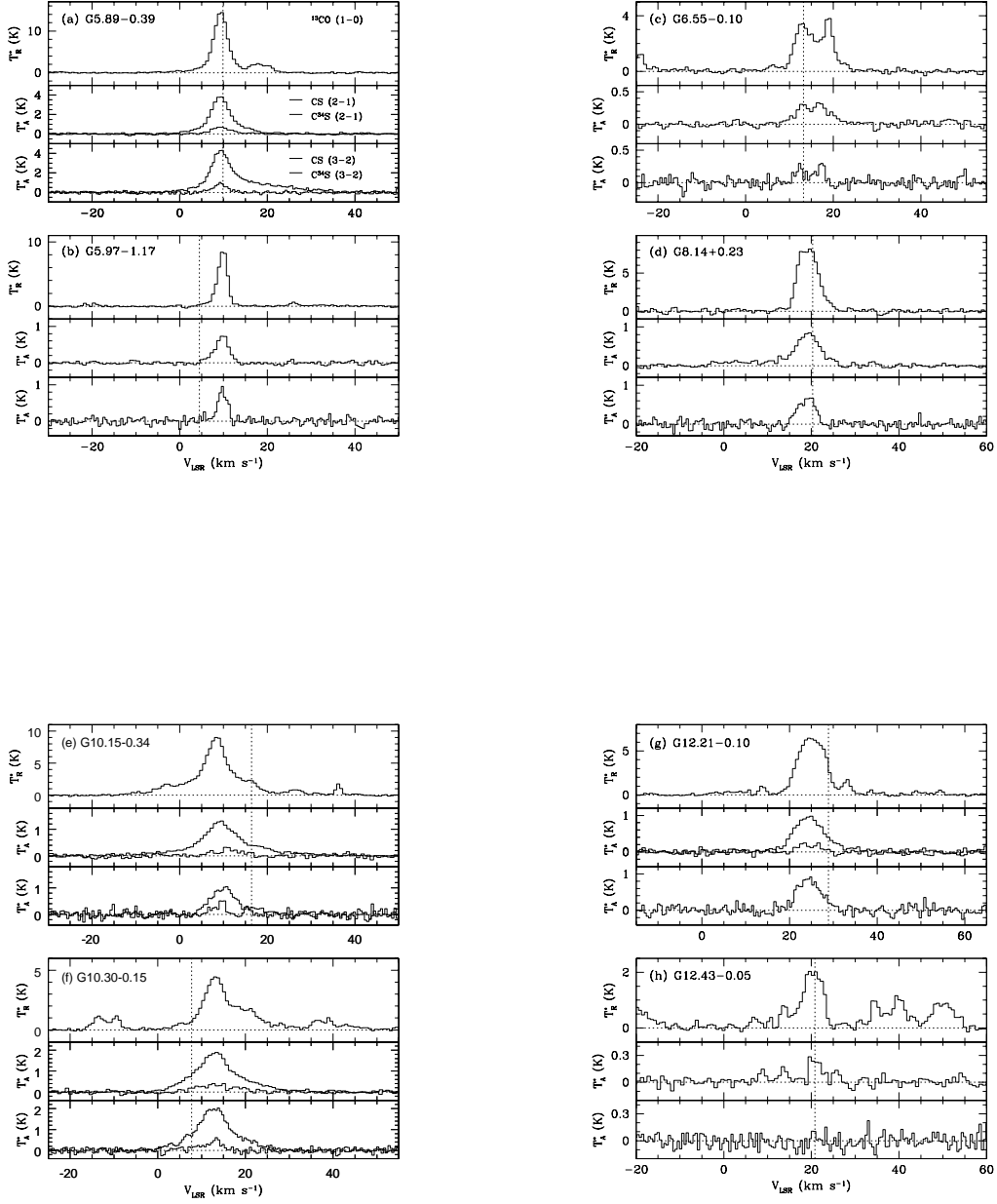


Fig. 1.— ^{13}CO , CS, and C^{34}S line profiles at the positions of UC HII regions. In each panel, the vertical dotted line represents the center velocity of H76 α line emission obtained in Paper I except for G12.43–0.05. It indicates the center velocity of NH_3 (2,2) line in G12.43–0.05 (1*h*).

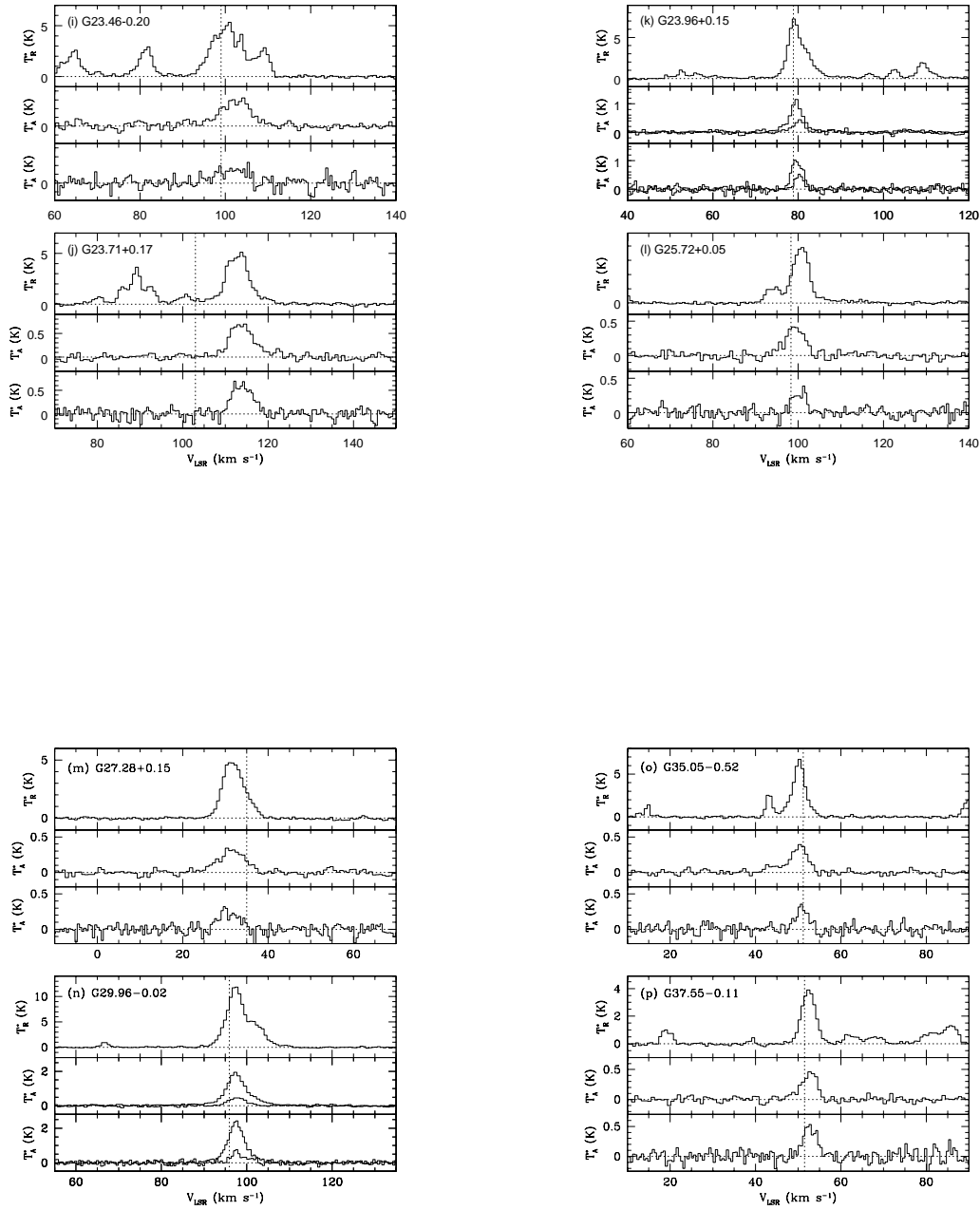


Fig. 1.—*Continued*

Fig. 2.— ^{13}CO J=1–0 line integrated intensity ($\int T_{\text{R}}^* dv$) maps. The integrated velocity range is presented at the top in each panel, while contour levels and grey scale flux range are listed at the bottom. Large crosses represent UC HII regions while small crosses indicate compact HII regions without UC HII regions (Paper I).

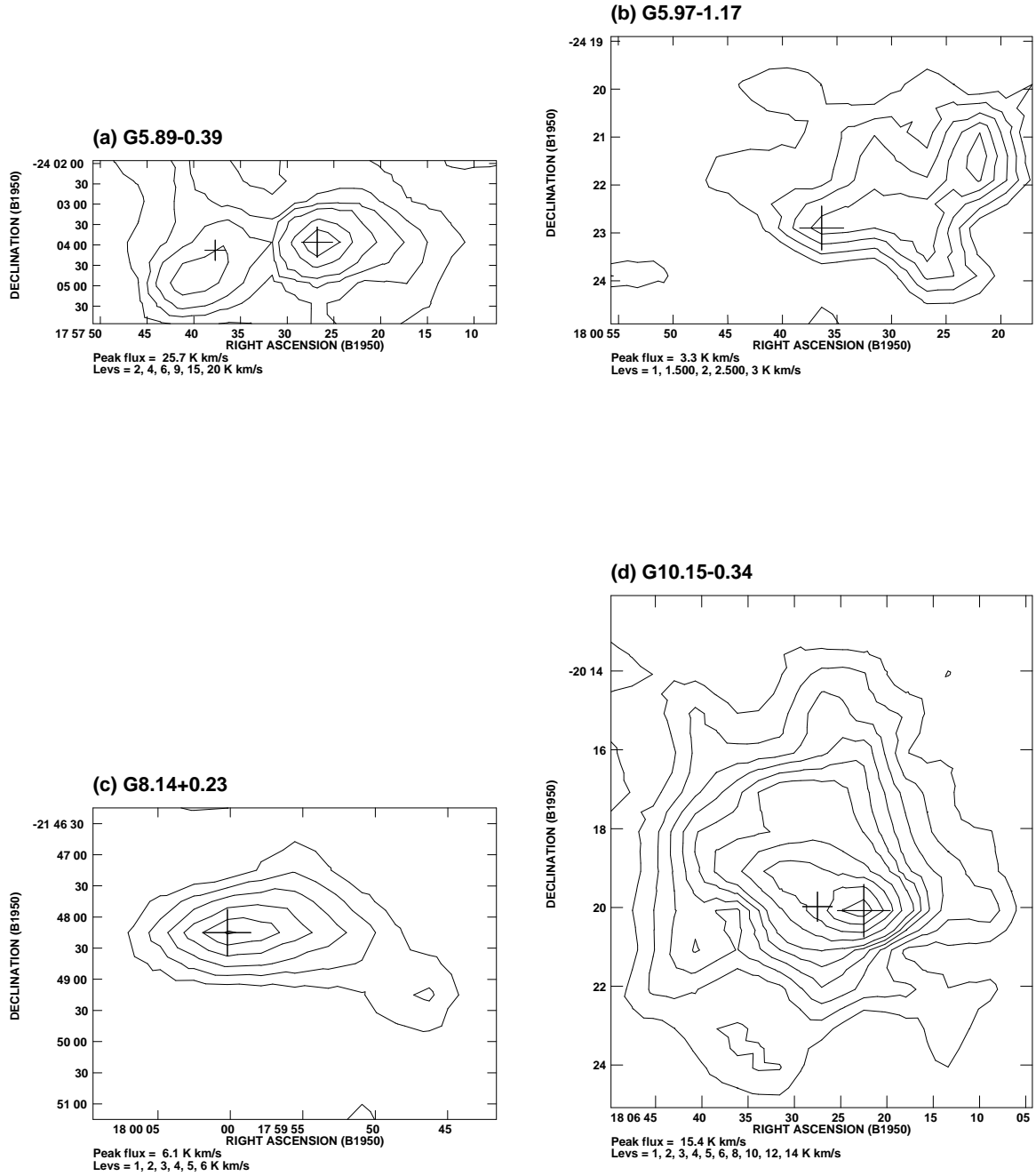


Fig. 3.— CS J=2–1 line integrated intensity ($\int T_A^* dv$) maps. Contour levels are shown at the bottom in each panel. Symbols are the same as in Figure 2.

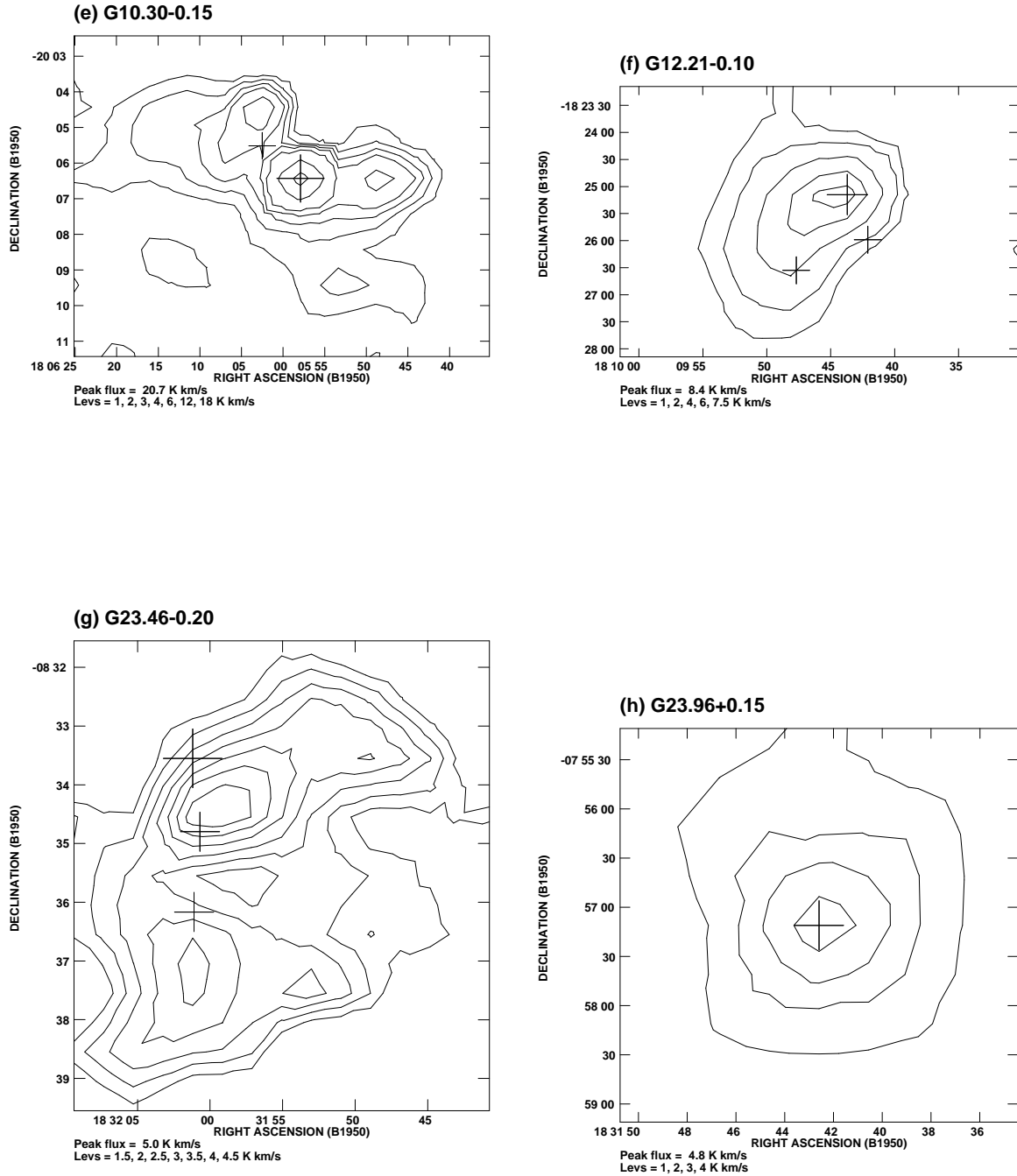


Fig. 3.—Continued

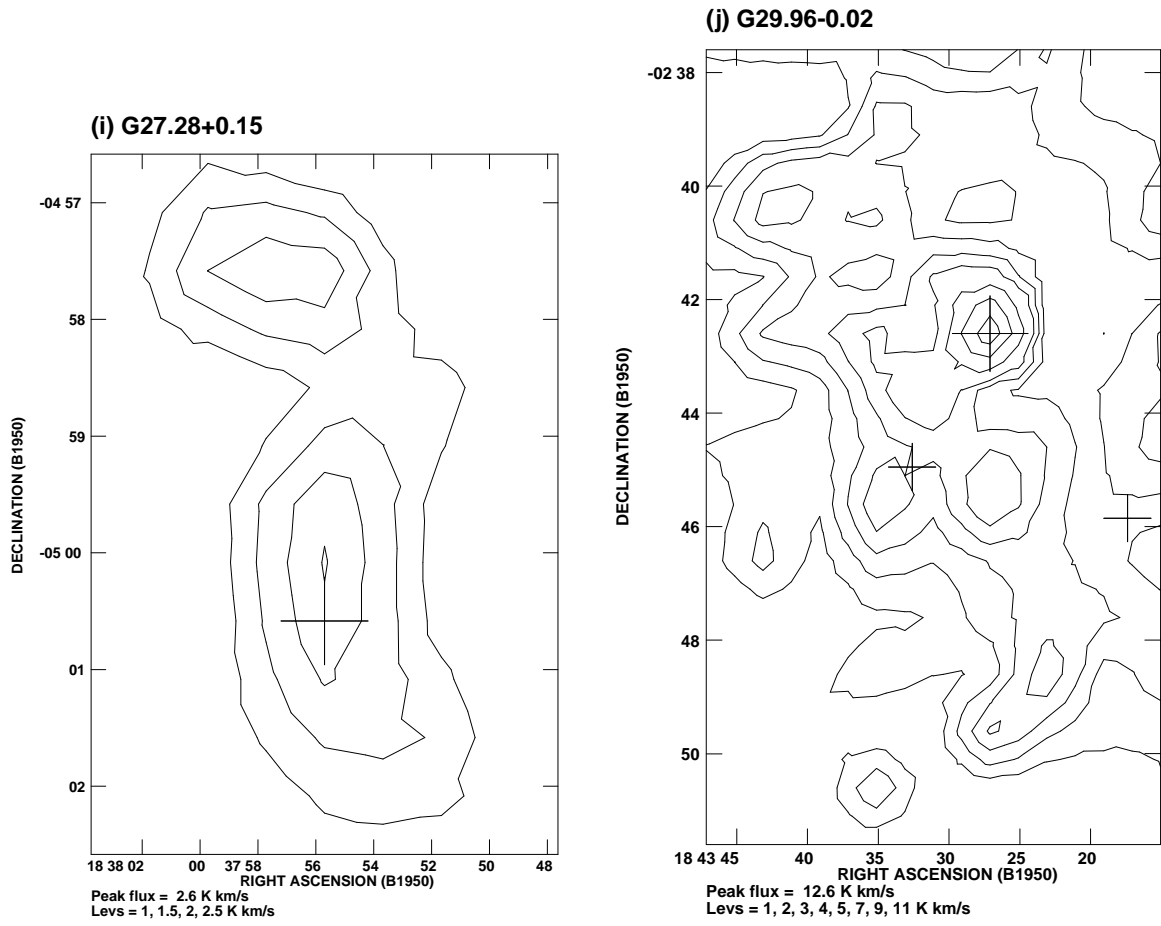


Fig. 3.—Continued

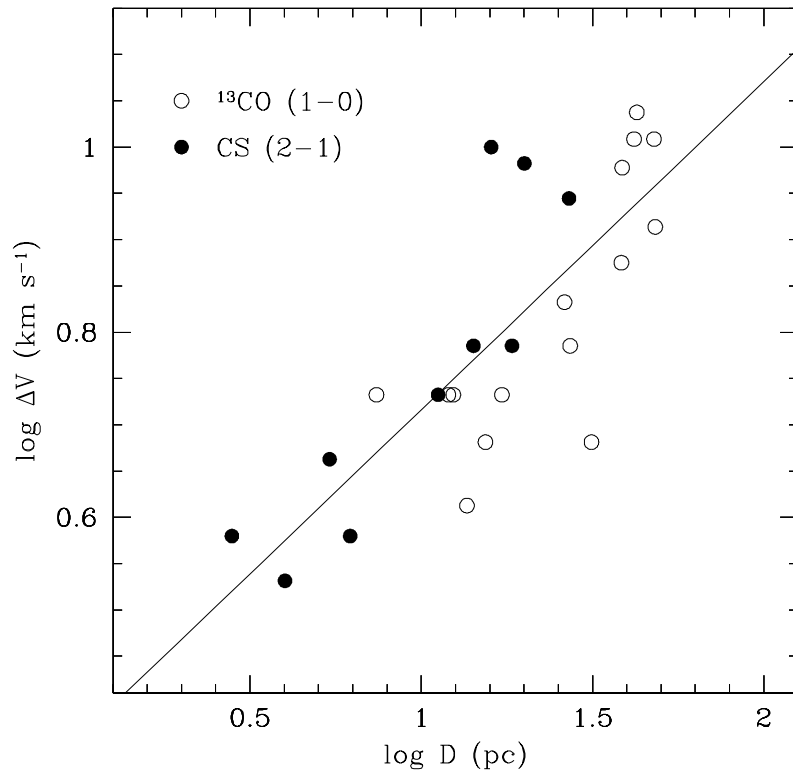


Fig. 4.— Plot of Δv against D . Open and filled circles indicate the data points estimated from ^{13}CO and CS line observations, respectively. There is a fairly good correlation between the two parameters. A linear fit to the data points gives $\log \Delta v = 0.35 \log D + 0.4$ with a correlation coefficient of 0.8. The solid line represents the fitted relation.

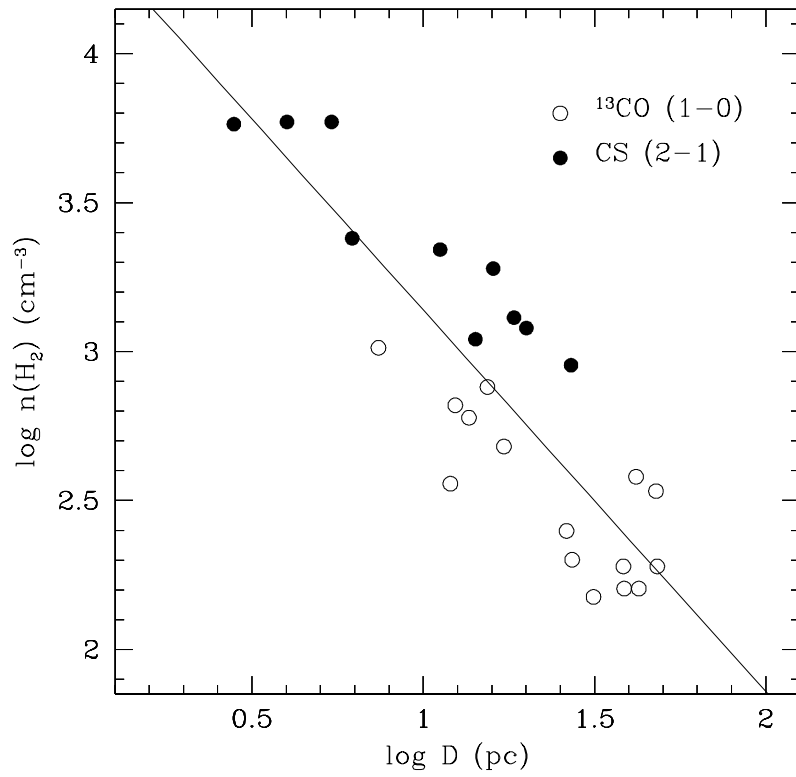


Fig. 5.— Comparison of $n(\text{H}_2)$ with D . A strong correlation is present between the two. Using a linear-squares fit we obtained $\log n(\text{H}_2) = -1.24 \log D + 4.4$, as shown by the solid line. Symbols are the same as in Figure 4.

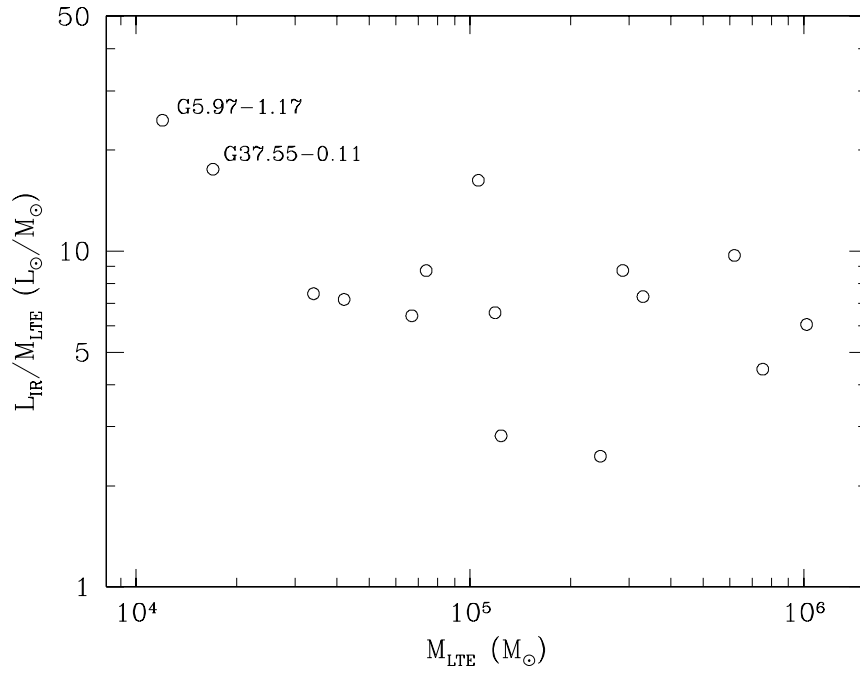


Fig. 6.— The $L_{\text{IR}}/M_{\text{LTE}}$ ratio versus M_{LTE} . We cannot see any apparent correlation between the two parameters.

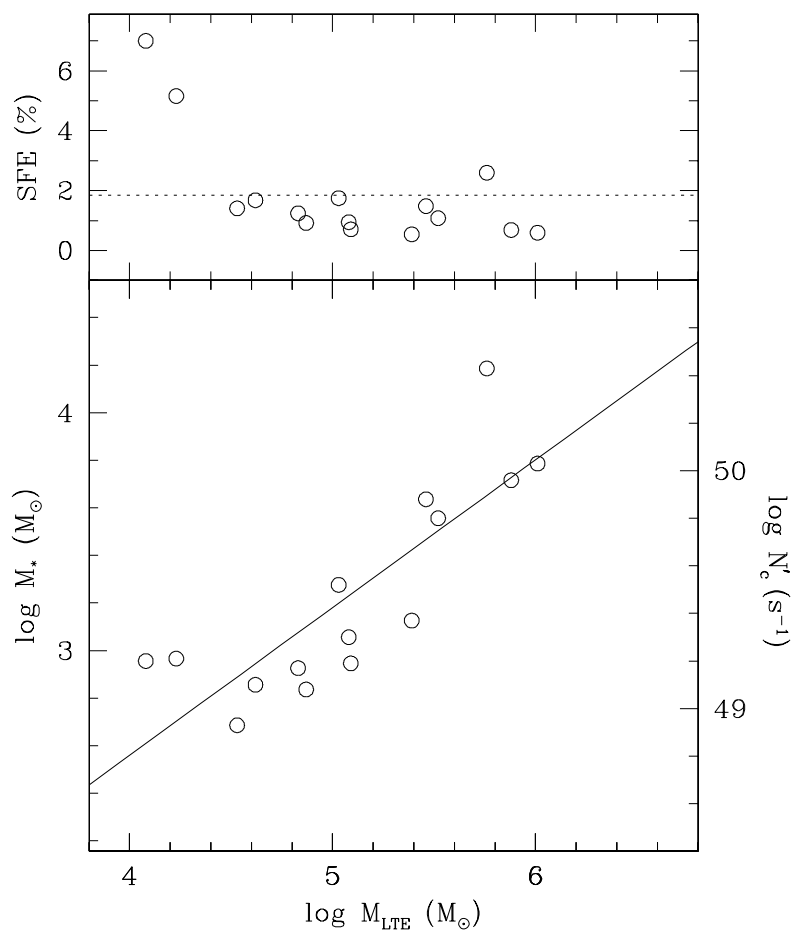


Fig. 7.— Stellar mass M_* , Lyman continuum photon flux N'_c (lower panel), and star formation efficiency (SFE) (upper panel) are compared with the cloud mass M_{LTE} . The solid line is the fitted relation in the lower panel. In the upper panel the dotted line indicates the average value of SFE, 1.9%.

Fig. 8.— ^{13}CO integrated intensity image (grey scale) and 21 cm radio continuum image (contour), made with the VLA DnC-array at about $40'' \times 20''$ angular resolution (Paper I). Grey scale flux ranges are the same as in Figure 2. Contour levels are listed at the bottom in each panel. Crosses represent the positions of UC HII regions. We can see in most sources that the UC and compact components of HII regions are associated with the dense cores of molecular clouds, while the diffuse extended envelopes often develop in the direction of decreasing molecular gas density (see the text for details).

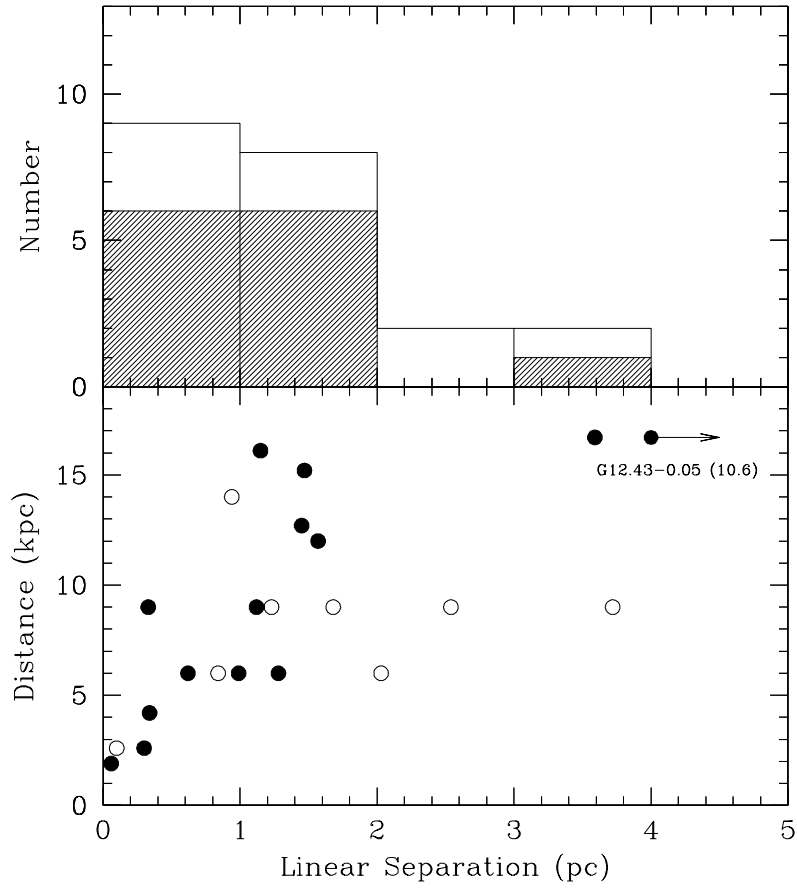


Fig. 9.— The projected linear separation between radio continuum peak and the nearest ^{13}CO peak. The lower panel exhibits a plot of the separation versus the distance. Here filled and open circles are compact HII regions with and without UC HII regions, respectively. The upper panel is a histogram showing the number of compact HII regions at each separation interval. Shaded blocks represent the number of compact HII regions with UC HII regions, while open blocks indicate the number of those without UC HII regions.

Table 1. ^{13}CO J=1–0 Line Observational Parameters

Source	$\alpha(1950)$ (^h ^m ^s)	$\delta(1950)$ (^o ' ^{''})	Map Center		Map Size $\theta_\alpha \times \theta_\delta$ (')	OFFs ^a (<i>l</i> , <i>b</i>) (^o)	Adopted ^b Distance (kpc)
			$\alpha(1950)$ (^h ^m ^s)	$\delta(1950)$ (^o ' ^{''})			
G5.89–0.39	17 57 26.8	–24 03 56	17 57 37.7	–24 03 51	20 × 20	(5.00, –2.00)	2.6
G5.97–1.17	18 00 36.4	–24 22 54	18 00 36.4	–24 22 54	20 × 20	(5.90, –1.50)	1.9
G6.55–0.10	17 57 47.4	–23 20 30	17 57 47.4	–23 20 30	10 × 10	(6.55, +1.50)	16.7
G8.14+0.23	18 00 00.2	–21 48 15	18 00 00.2	–21 48 15	20 × 15	(9.00, +0.50)	4.2
G10.15–0.34 ...	18 06 22.5	–20 20 05	18 06 09.1	–20 09 23	30 × 40	(10.15, –1.50)	6.0
G10.30–0.15 ...	18 05 57.9	–20 06 26	"	"	"	"	6.0
G12.21–0.10 ...	18 09 43.7	–18 25 09	18 09 43.7	–18 25 09	20 × 10	(12.00, +1.00)	16.1
G12.43–0.05 ...	18 09 58.9	–18 11 58	18 09 58.9	–18 11 58	7 × 7	(12.00, +1.00)	16.7
G23.46–0.20 ...	18 32 01.2	–08 33 33	18 32 00.0	–08 35 00	15 × 15	(22.86, –0.86)	9.0
G23.71+0.17 ...	18 31 10.3	–08 09 36	18 31 10.3	–08 09 36	9 × 7	(23.87, +0.83)	9.0
G23.96+0.15 ...	18 31 42.6	–07 57 11	18 31 42.6	–07 57 11	9 × 7	(23.87, +0.83)	6.0
G25.72+0.05 ...	18 35 21.6	–06 26 27	18 35 28.0	–06 27 00	10 × 7	(25.66, –1.00)	14.0
G27.28+0.15 ...	18 37 55.7	–05 00 35	18 37 55.7	–05 00 35	10 × 7	(26.94, –0.50)	15.2
G29.96–0.02 ...	18 43 27.1	–02 42 36	18 43 30.8	–02 45 10	20 × 15	(30.00, +0.50)	9.0
G35.05–0.52 ...	18 54 37.1	+01 35 01	18 54 37.1	+01 35 01	13 × 7	(34.10, –1.00)	12.7
G37.55–0.11 ...	18 57 46.8	+03 59 00	18 57 46.8	+03 59 00	7 × 7	(37.55, –0.50)	12.0

^aReference positions with some ^{13}CO emission (see the text).

^bFrom references given by Wood & Churchwell (1989).

Table 2. ^{13}CO J=1–0 Line Observational Result

Source	W_{\circ} (K km s $^{-1}$)	R (pc)	M_{LTE} ($10^4 M_{\odot}$)	$n(\text{H}_2)$ (10^2 cm^{-3})	Δv^{a} (km s $^{-1}$)
G5.89–0.39	15	7.7	7.4	7.6	4.8
G5.97–1.17	10	3.7	1.2	10.3	4.8
G6.55–0.10	10	21.4	33.0	1.6	9.9
G8.14+0.23	10	6.8	4.2	6.0	4.1
G10.15–0.30 ...	10	24.1	57.5	1.9	8.2
G12.21–0.10 ...	10	19.2	28.7	1.9	7.5
G12.43–0.05 ...	10	15.7	12.4	1.5	4.8
G23.46–0.20 ...	15	20.9	75.4	3.8	10.2
G23.71+0.17 ...	15	8.6	6.7	4.8	5.8
G23.96+0.15 ...	10	6.2	3.4	6.6	5.1
G25.72+0.05 ...	10	13.6	10.6	2.0	5.4
G27.28+0.15 ...	10	13.1	11.9	2.5	6.8
G29.96–0.02 ...	20	23.9	102.0	3.4	10.2
G35.05–0.52 ...	10	19.3	24.6	1.6	9.5
G37.55–0.11 ...	10	6.0	1.7	3.6	4.8

^aFWHM of the average spectrum of the entire mapping area.

Table 3. CS Line Parameters

Source	OFFs (l, b) ($^{\circ}$)	CS (2–1)					CS (3–2)		
		v_{LSR} (km s^{-1})	T_{A}^* (K)	Δv (km s^{-1})	$\int T_{\text{A}}^* dv$ (K km s^{-1})	$N(\text{CS})$ (10^{13} cm^{-2})	v_{LSR} (km s^{-1})	T_{A}^* (K)	Δv (km s^{-1})
G5.89–0.39	(5.00, –1.00)	9.6	3.80	6.1	25.9	44.0	9.8	4.30	5.6
G5.97–1.17	(5.00, –1.00)	9.6	0.73	3.4	2.8	4.7	9.8	0.95	2.3
G6.55–0.10	(7.00, –1.00)	15.0	0.33	6.9	2.6	4.4	14.3	0.30	6.6
G8.14+0.23	(8.60, +0.60)	19.6	0.85	6.1	6.2	10.4	19.8	0.67	5.1
G10.15–0.34 ...	(10.15, +0.50)	9.6	1.31	8.8	16.6	28.1	10.8	1.05	7.1
G10.30–0.15 ...	(10.15, +0.50)	13.5	1.90	8.8	21.8	37.0	13.8	2.00	7.7
G12.21–0.10 ...	(12.21, +0.50)	25.0	0.98	8.0	8.4	14.2	24.9	0.91	6.4
G12.43–0.05 ...	(12.21, +0.50)	19.6	0.28	3.1	1.2	2.0	...	<0.1	...
G23.46–0.20 ...	(23.46, +0.50)	101.9	0.30	7.7	2.8	4.7	102.8	0.17	7.1
G23.71+0.17 ...	(23.80, +0.50)	114.6	0.70	6.1	5.1	8.7	114.2	0.60	5.6
G23.96+0.15 ...	(23.80, +0.50)	79.6	1.15	2.7	4.8	8.2	79.2	1.02	3.6
G25.72+0.05 ...	(25.65, –0.60)	98.9	0.42	5.4	2.3	3.9	101.3	0.28	4.1
G27.28+0.15 ...	(27.30, –0.50)	30.4	0.34	5.4	2.4	4.2	29.8	0.30	4.6
G29.96–0.02 ...	(30.00, +0.50)	97.3	1.94	5.0	12.4	21.1	97.7	2.41	4.1
G35.05–0.52 ...	(35.15, –1.00)	51.1	0.40	3.8	2.1	3.6	50.8	0.35	2.8
G37.55–0.11 ...	(37.55, –0.50)	52.7	0.46	4.2	2.0	3.5	52.8	0.53	3.6

Table 4. C³⁴S Line Parameters

Source	C ³⁴ S (2–1)				C ³⁴ S (3–2)			
	v_{LSR} (km s ⁻¹)	T_{A}^* (K)	Δv (km s ⁻¹)	τ_{p}	v_{LSR} (km s ⁻¹)	T_{A}^* (K)	Δv (km s ⁻¹)	τ_{p}
G5.89–0.39	9.6	0.70	5.4	0.26	9.2	1.03	3.1	0.35
G10.15–0.34 ...	10.4	0.32	3.1	0.36	10.3	0.50	2.6	0.88
G10.30–0.15 ...	15.1	0.40	7.0	0.30	13.4	0.62	2.1	0.48
G12.21–0.10 ...	23.5	0.25	4.7	0.38	...	<0.10	...	<0.14
G23.96+0.15 ...	80.4	0.44	2.3	0.64	80.3	0.52	2.6	0.97
G29.96–0.02 ...	98.1	0.46	4.7	0.35	97.7	0.75	2.1	0.48

Table 5. Properties of CS Clouds

Source	R (pc)	M_{LTE} ($10^4 M_{\odot}$)	$n(\text{H}_2)$ (10^3 cm^{-3})	Δv^{a} (km s^{-1})	Fraction ^b	
					Area (%)	Mass (%)
G5.89–0.39	2.7	2.6	5.9	4.6	12	35
G5.97–1.17	1.4	0.3	5.8	3.8	14	25
G8.14+0.23	2.0	1.0	5.9	3.4	9	24
G10.15–0.34 ...	8.0	21.3	1.9	10.0	16	48
G10.30–0.15 ^c ...	5.6	8.2	2.2	5.4	"	"
G12.21–0.10 ...	9.2	21.4	1.3	6.1	23	75
G23.46–0.20 ...	10.0	25.1	1.2	9.6	23	33
G23.96+0.15 ...	3.1	1.6	2.4	3.8	25	47
G27.28+0.15 ...	7.1	8.5	1.1	6.1	29	71
G29.96–0.02 ...	13.5	47.1	0.9	8.8	32	46

^aFWHM of the average spectrum of the entire mapping area.

^bFraction of CS parameter relative to ^{13}CO parameter.

^cIncluded with G10.15–0.34 to calculate the fraction values.

Table 6. Star Formation Activity of Molecular Clouds

Source	$R(\overline{T}_d, \beta)$	L_{IR} ($10^5 L_{\odot}$)	$L_{\text{IR}}/M_{\text{LTE}}$ (L_{\odot}/M_{\odot})	$\log N_c'^{\text{a}}$ (s^{-1})	M_*^{b} ($10^2 M_{\odot}$)	SFE (%)
G5.89–0.39	1.37	6.5	8.8	49.08	6.9	0.9
G5.97–1.17	1.41	2.9	24.5	49.20	9.0	7.0
G6.55–0.10	1.38	24.2	7.3	49.80	36.0	1.1
G8.14+0.23	1.37	3.0	7.2	49.10	7.2	1.7
G10.15–0.30 ...	1.36	60.2	9.7	50.43	153.4	2.6
G12.21–0.10 ...	1.40	25.1	8.8	49.88	43.2	1.5
G12.43–0.05 ...	1.67	3.5	2.8	49.19	8.8	0.7
G23.46–0.20 ...	1.48	33.6	4.5	49.96	52.0	0.7
G23.71+0.17 ...	1.36	4.3	6.4	49.17	8.4	1.2
G23.96+0.15 ...	1.36	2.5	7.5	48.97	4.9	1.4
G25.72+0.05 ...	1.36	17.2	16.3	49.52	18.9	1.7
G27.28+0.15 ...	1.42	7.8	6.6	49.30	11.4	0.9
G29.96–0.02 ...	1.36	61.7	6.1	50.03	61.1	0.6
G35.05–0.52 ...	1.38	6.0	2.5	49.37	13.4	0.5
G37.55–0.11 ...	1.36	3.0	17.5	49.21	9.2	5.2

^aTaken from Paper I.

^bSee § 4.1.

This figure "f2_abcd.jpg" is available in "jpg" format from:

<http://arxiv.org/ps/astro-ph/0306405v1>

This figure "f2_efgh.jpg" is available in "jpg" format from:

<http://arxiv.org/ps/astro-ph/0306405v1>

This figure "f2_ijkl.jpg" is available in "jpg" format from:

<http://arxiv.org/ps/astro-ph/0306405v1>

This figure "f2_mno.jpg" is available in "jpg" format from:

<http://arxiv.org/ps/astro-ph/0306405v1>

This figure "f8_abcd.jpg" is available in "jpg" format from:

<http://arxiv.org/ps/astro-ph/0306405v1>

This figure "f8_efgh.jpg" is available in "jpg" format from:

<http://arxiv.org/ps/astro-ph/0306405v1>

This figure "f8_ijkl.jpg" is available in "jpg" format from:

<http://arxiv.org/ps/astro-ph/0306405v1>

This figure "f8_mno.jpg" is available in "jpg" format from:

<http://arxiv.org/ps/astro-ph/0306405v1>